https://doi.org/10.5194/essd-2026-520
Preprint. Discussion started: 27 July 2026

Open Access Earth System Science Data Discussions

A Global Paired Argo Dataset for Ocean Thermal and Salinity Responses to Tropical Cyclones (2000–2024)

Xiuting Wang[1, 2], Han Zhang[2, 3, 4, *], Mengyuan Xu[5], Tao Lian[1, 2, 3, *], Jiagen Li[6], Di Tian[2], Jie Yu[7]

1 Ocean College, Zhejiang University, Zhoushan 316021, China

2 State Key Laboratory of Satellite Ocean Environment Dynamics, Second Institute of Oceanography, Ministry of Natural Resources, Hangzhou 310012, China

3 Southern Marine Science and Engineering Guangdong Laboratory (Zhuhai), Zhuhai 519082, China

4 CMA-FDU Joint Laboratory of Marine Meteorology, Shanghai 200438, China

5 Hangzhou Meteorological Technology Development Company, Hangzhou, 310008, China

6 College of Meteorology and Oceanography, National University of Defense Technology, Changsha, 410073, China

7 School of Marine Science, Sun Yat-sen University and Southern Marine Science and Engineering Guangdong Laboratory (Zhuhai), Zhuhai, China.

* Corresponding author: zhanghan@sio.org.cn (Han Zhang), liantao@sio.org.cn (Tao Lian)

Abstract

This paper presents a global paired Argo dataset documenting the upper-ocean temperature and salinity responses to tropical cyclones (TCs) during 2000–2024. The dataset was built by combining the International Best Track Archive for Climate Stewardship (IBTrACS, v04r01) with the Global Ocean Argo Scatter Dataset (Version 3.0) provided by the China Argo Real-time Data Center. On top of the original Argo quality-control flags, we applied a strict secondary screening that retained only profiles with good quality flags for temperature, salinity, and pressure at every vertical level and with a maximum sampling depth of at least 1900 m. Each TC location was first matched to candidate floats within an inclusive 1000 km search envelope, with the archived storm-relative coordinates allowing users to apply narrower distance thresholds for specific analyses. The two profiles in each pair were further required to lie within 50 km of each other to suppress horizontal mesoscale aliasing. All retained profiles were linearly interpolated onto 56 standard depth levels from the surface to 2000 m and rotated into a storm-relative Cartesian frame in which the TC center is the origin and the translation direction is aligned with the positive Y axis. The final product contains 3164876 high-quality paired records—2747731 in the

https://doi.org/10.5194/essd-2026-520
Preprint. Discussion started: 27 July 2026

Northern Hemisphere and 417145 in the Southern Hemisphere—archived as six self-describing netCDF files separated by hemisphere and time period. Spatial, vertical, and temporal composites confirm that the dataset reproduces the canonical upper-ocean response to TCs, including the hemispheric mirror asymmetry of cross-track surface cooling, the concentration of the strongest thermal anomalies within the upper ~200 m, and a peak sea surface cooling about 2.5 d after passage followed by a 1–2 week recovery. The salinity response is weaker and less spatially coherent, reflecting the competing effects of rainfall freshening, vertical mixing, and upwelling. By providing background-field profiles, response-field profiles, and their precomputed differences in a single analysis-ready record, this dataset substantially reduces the preprocessing burden for studies of TC–ocean interaction, upper-ocean heat and salt budgets, mixed-layer and near-inertial processes, and the evaluation of coupled ocean–atmosphere models. The dataset and associated data-generation code are available at https://doi.org/10.6084/m9.figshare.32820563 (Wang et al., 2026b).

1 Introduction

Tropical cyclones (TCs) are among the most energetic air–sea coupled phenomena on Earth, and their passage rapidly reorganizes the thermal and haline structure of the upper ocean (Xu et al., 2024; Falor et al., 2024; DeMaria et al., 2013). Strong TC winds drive near-inertial shear, entrainment, and Ekman-pumping-induced upwelling that cool the sea surface, warm the subsurface, and modify surface salinity, with these changes in turn feeding back on storm intensity, air–sea heat and moisture fluxes, mixed-layer depth, and the subsequent re-stratification of the upper ocean (Zhang et al., 2021; Jacob et al., 2000; Shay, 2010; Price, 1981; Shay et al., 2011; Qiu et al., 2019). Recent modeling work further shows that storm size, commonly represented by the 34-kt wind radius, can strongly modulate both the magnitude and spatial extent of TC-induced SST cooling, with vertical mixing remaining the dominant cooling process (Liu et al., 2025). Because these responses couple directly to storm intensification, ocean heat uptake, and transient upper-ocean variability (Wang et al., 2016; Wang et al., 2022; Jiang et al., 2023), a systematic, globally distributed observational description of the paired background- and response-field ocean state is essential for both process studies and the evaluation of coupled ocean–atmosphere models. Recent drifter-based analyses further show that storm-local SSTs beneath TCs are warming rapidly and

https://doi.org/10.5194/essd-2026-520
Preprint. Discussion started: 27 July 2026

that in situ estimates of TC-induced inner-core cooling can be substantially weaker than microwave-satellite estimates, underscoring the need for reliable in situ benchmarks of TC–ocean feedbacks (Guan et al., 2026).

No single observing platform can produce such a description on its own. Satellite remote sensing provides near-global and temporally continuous coverage, but it is fundamentally restricted to the ocean surface and cannot directly resolve the vertical temperature and salinity structure that governs the TC-induced response (Sun et al., 2021b; Stiles et al., 2020). Moored arrays, research cruises, airborne expendable probes, unmanned platforms, and targeted field campaigns have produced some of the most detailed process-level insights into TC–ocean interaction (Zhang et al., 2016; Aberson et al., 2006; Zhang et al., 2024a). Recent moored-array data products from the northern South China Sea, including the MASCS 1.0 cross-shaped array during 2014–2015 and a triangle-shaped array during 2016, further demonstrate the value of synchronous atmospheric and oceanic observations for resolving air–sea fluxes, internal waves, low-frequency flows, and TC-related ocean responses (Zhang et al., 2024a; Zhang et al., 2026; Zhao et al., 2025; Zhang et al., 2024b). Nevertheless, such observations are typically concentrated in specific basins, arrays, or storms, and are therefore too sparse to sustain a unified multi-storm statistical synthesis at the global scale (Stiles et al., 2020; Rogers, 2021; Hristova-Veleva et al., 2020). Consequently, a long-term, globally distributed three-dimensional characterization of the TC-induced ocean response continues to rely on profile-based in situ observations capable of resolving both temperature and salinity from the surface into the main thermocline and below (Domingues et al., 2019; Hu et al., 2024).

The global Argo array has fundamentally changed this situation by providing standardized, quasi-uniformly distributed temperature and salinity profiles from the sea surface to 2000 m (Jayne et al., 2017; Roemmich et al., 2019). Its long-term, multi-decadal, multidisciplinary coverage has enabled studies of TC–ocean interaction to transition from individual case analyses to genuinely statistical, global-scale investigations (Roemmich et al., 2019; Roemmich et al., 2009; Liu et al., 2021). Using Argo data, Cheng et al. (2015) produced an early global footprint of TC-induced upper-ocean thermal change by compositing background- and response-field profiles. More recent analyses have extended such approaches to explicitly resolve hemispheric contrasts, salinity variability, and the stratification-dependent response (Han et al., 2024, 2025; Sala et al., 2024; Steffen and Bourassa, 2018), while

https://doi.org/10.5194/essd-2026-520
Preprint. Discussion started: 27 July 2026

Open Access Earth System Science Data Discussions

complementary satellite and in situ studies have shown that the salinity signature, though noisier than the thermal one, carries first-order information about rainfall freshening, vertical mixing, upwelling, horizontal advection, and barrier-layer modulation of storm intensification (Balaguru et al., 2012; Reul et al., 2021; Guan et al., 2025).

Despite this progress, what the community has accumulated so far is mostly a set of published research results rather than a reusable data product. First, the majority of Argo-based TC–ocean studies stop at the stage of composite analysis, and the underlying paired records are seldom released in an analysis-ready form that subsequent users can directly ingest (Cheng et al., 2015). Second, the focus of existing work is heavily skewed toward the thermal response, so a systematic archive that documents temperature and salinity responses with equal rigour — and that preserves the full background- and response-field profile pairs rather than only derived composites — is still lacking (Park et al., 2023). Third, existing studies differ substantially in their choice of time span, search radius, pairing time windows, quality control thresholds, and definitions of the storm-relative coordinate system (DeMaria et al., 2013). These methodological inconsistencies make it difficult for users to cross-compare results or to build cumulative knowledge across the literature. As a result, researchers who wish to perform their own composite analyses, heat- and salt-budget estimates, or model evaluations currently have to repeat the full workflow of profile screening, spatiotemporal pairing, interpolation, and coordinate transformation — an effort that consumes a disproportionate share of each new study.

Motivated by this gap, we present a global paired Argo dataset of ocean temperature and salinity responses to tropical cyclones for 2000–2024, constructed by combining the IBTrACS best-track archive (Knapp et al., 2010) with the Global Ocean Argo Scatter Dataset (Version 3.0) provided by the China Argo Real-time Data Center. On top of the original Argo quality-control flags we apply a strict secondary screening, and we adopt a uniform spatiotemporal pairing protocol that associates each TC location with its matched background-field and response-field profiles. All retained profiles are interpolated onto 56 standard levels from the surface to 2000 m and transformed into a storm-relative coordinate system to enable direct composite analysis. The final product is archived as six netCDF files split by hemisphere and by period, with background-field profiles, response-field profiles, and their precomputed differences all provided in a single record, so that users can proceed directly to scientific analysis without repeating

https://doi.org/10.5194/essd-2026-520
Preprint. Discussion started: 27 July 2026

the download, screening, pairing, or preprocessing themselves. This dataset is intended to reduce the substantial effort required for screening, pairing, and preprocessing in situ observations, and to provide an analysis-ready benchmark for studies of TC–ocean interaction, upper-ocean heat and salt changes, mixed-layer and near-inertial processes, and the evaluation of coupled air–sea models.

2 Dataset description

2.1 Data source

The global TC best-track data used in this study were obtained from the International Best Track Archive for Climate Stewardship (IBTrACS) version v04r01 (Knapp et al., 2010; Gahtan et al., 2024). To accurately characterize TC properties and trajectories, the storm center coordinates, maximum sustained wind speed, translation speed, and translation direction were extracted at 3-hour intervals for the period 2000–2024. In the paired Argo netCDF files, the Wind variable preferentially adopts USA_WIND from IBTrACS; when USA_WIND is missing, it is supplemented with TOKYO_WIND, which is converted from a 10-min sustained wind to an equivalent 1-min maximum sustained wind following Harper et al. (2010).

The corresponding ocean profile data were acquired from the Global Ocean Argo Scatter Dataset (Version 3.0), provided by the China Argo Real-time Data Center (CARDC). CARDC operationally aggregates temperature, salinity, and pressure measurements from autonomous profiling floats deployed worldwide and applies a standardized real-time and delayed-mode quality-control protocol consistent with the international Argo program (Wong et al., 2020). The combination of these two independent datasets enables a globally consistent identification of paired Argo profiles along TC tracks and supports a uniform investigation of the associated thermal and haline responses. Detailed definitions of all archived variables are provided in Table S5 of the Supplementary Material.

2.2 Quality control and Argo pairing workflow

Constructing the paired record set required that every retained profile (i) sampled most of the upper 2000 m water column, with the deepest valid measurement reaching at least 1900 m; values on the standard depth grid were then obtained by linear interpolation, with limited extrapolation applied near the deepest

https://doi.org/10.5194/essd-2026-520
Preprint. Discussion started: 27 July 2026

levels where necessary; (ii) carried reliable temperature and salinity values at every standard level; and (iii) was matched to a single TC location through both a background-field and a response-field observation that satisfied the prescribed spatiotemporal pairing criteria. The workflow used to enforce these requirements is summarized in Fig. 1; it combines profile-level screening with a spatiotemporal pairing protocol.

CARDC profiles are already subject to the standard real-time and delayed-mode quality control of the international Argo program. We then applied two further filters. First, a profile was kept only if its temperature, salinity, and pressure quality-control flags equaled 1 ("good") at every vertical level from the surface to the deepest observation. The definitions of the quality-control flags are provided in the ARGO User's Manual, Version 3.44.0 (Argo data management, 2025). Profiles containing any non-1 flag, any sentinel fill value (e.g., -999.999), or any missing record at any level were discarded as a whole; partial truncation would otherwise have introduced depth-dependent sampling biases into the subsequent vertical compositing. Second, only profiles whose deepest valid measurement reached at least 1900 m were retained, so that the surface mixed layer, the main thermocline, and the upper intermediate water could be analyzed on a common vertical grid.

Profiles passing this screening were matched to IBTrACS TC track points, which are recorded at 3 h intervals for 2000–2024. In this pairing step, we retained all available IBTrACS TC location points rather than preselecting cases by storm intensity, storm size, basin, or life-cycle stage. The purpose of this inclusive design was to preserve a broad parent archive and to maximize the number of potential TC–Argo pairs. Users can therefore apply their own filters after downloading the dataset, for example by TC intensity, radial distance, relative time, basin, or other criteria suited to their specific applications. For each TC location, all qualified profiles within 1000 km of the storm center were taken as candidates. The 1000 km radius was used as an inclusive search envelope rather than as a prescribed analysis scale. Our aim was to retain a broad parent set of potentially relevant TC–Argo matches, while leaving users free to impose stricter distance criteria for their own applications. To support this flexibility, the archived files include the storm-relative cross-track and along-track coordinates of both the background-field and response-field profiles, so that users can readily subset the records by radial distance, cross-track distance, along-track distance, or any combination of these variables. Thus, the 1000 km threshold defines the

https://doi.org/10.5194/essd-2026-520
Preprint. Discussion started: 27 July 2026

outer boundary of the archive, not the spatial scale at which all subsequent analyses must be performed. Earlier studies have sometimes used a dynamic radius scaled to the 50-knot wind extent, but that field is largely missing from pre-2003 IBTrACS records, particularly in the Southern Hemisphere; a fixed 1000 km radius therefore preserves the early years and yields continuous global coverage. Two non-overlapping temporal windows were then defined relative to TC passage. The background-field window covers 10 to 4 days prior to passage and is intended to capture an undisturbed background state, free of contamination by the storm's outer rainbands or peripheral winds. The response-field window covers 3 days prior to 35 days after passage, long enough to span both the earliest ocean adjustment and the subsequent multi-week recovery. We therefore refer to this second window as the response field rather than as a field defined only by samples following TC passage. A TC location was accepted as a candidate only when at least one profile fell within each window.

For every surviving candidate pair, the great-circle distance between the background-field and response-field observation locations was further required to be less than 50 km. This spatial proximity criterion was used to reduce the influence of horizontal sampling differences and mesoscale variability on the paired anomalies (Wu and Chen, 2012).

Starting from 2910954 raw Argo profiles archived between January 1999 and February 2025, the workflow produced 3164876 paired records, each consisting of one background-field profile and one response-field profile associated with a single TC location. The background-field screening retained 1027158 unique Argo profiles, while the response-field screening retained 2207518 unique Argo profiles. Because the same Argo profile can be matched to multiple TC location points, the final number of Argo pairs is larger than the number of raw Argo profiles. Each retained pair was then transformed into a TC-relative Cartesian frame and interpolated onto a common 56-level vertical grid, as described in Sect. 2.3.

https://doi.org/10.5194/essd-2026-520
Preprint. Discussion started: 27 July 2026

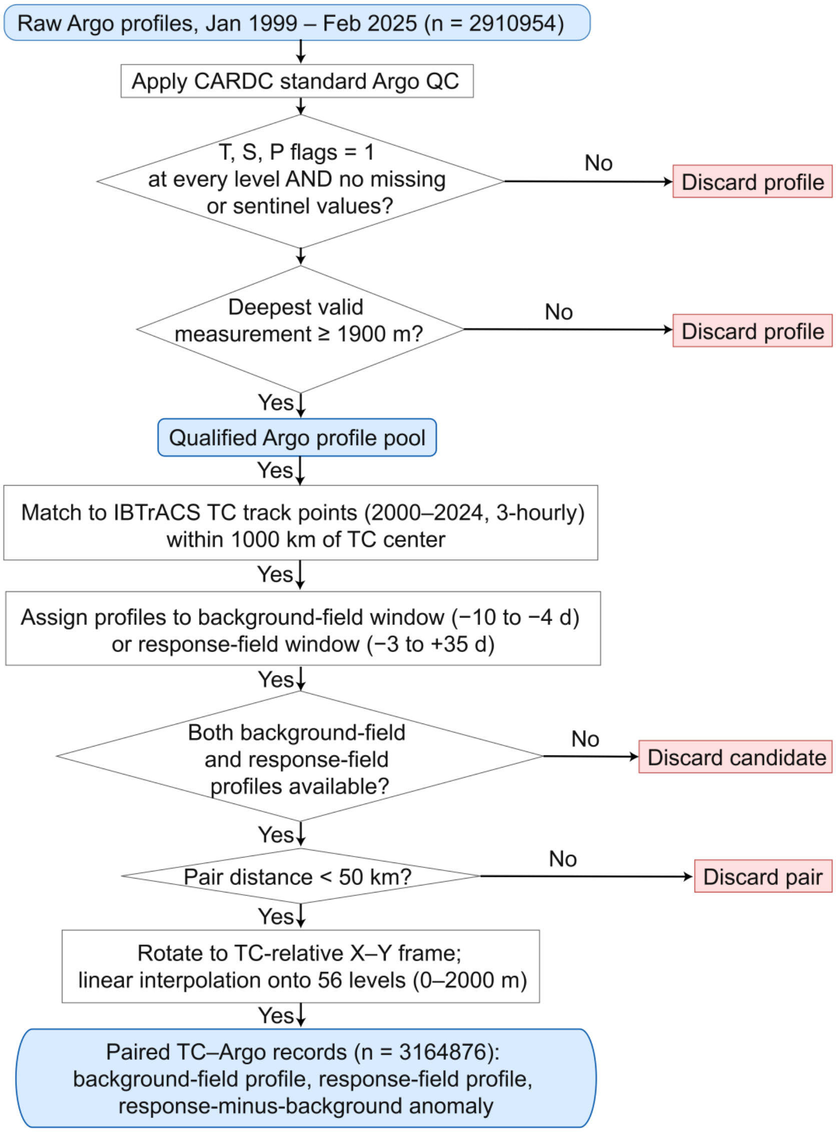

Figure 1. Flowchart of the data quality control and Argo–TC pairing workflow used to construct the paired Argo dataset. The upper portion shows the per-profile quality control procedure that yields the qualified Argo profile pool, and the lower portion shows the spatiotemporal pairing procedure that produces the final paired TC–Argo records. White rectangles denote filtering or processing steps, gray diamonds denote decision points, and blue capsules highlight the qualified profile pool and the final paired record set. In the quality control decision

https://doi.org/10.5194/essd-2026-520
Preprint. Discussion started: 27 July 2026

diamonds, T, S, and P denote the temperature, salinity, and pressure profiles, respectively, and "flag" refers to the per-observation quality indicator variable archived in the original Argo data files.

2.3 Coordinate rotation and variable interpolation

To standardize the analytical framework and to expose well-known features such as the rightward (leftward) bias of the cooling response in the Northern (Southern) Hemisphere, the original geographic coordinates of each retained Argo float were transformed into a TC-relative Cartesian frame. For every paired record, the longitudinal and latitudinal offsets between the float and the TC center were first computed; this relative position vector was then rotated clockwise so that the instantaneous TC translation direction coincides with the positive Y axis (i.e., due north in the rotated frame). After the rotation, the new coordinate variables X and Y (Table S5) represent the cross-track and along-track distances, respectively, with the TC center fixed at the origin. This rotation removes the heterogeneity introduced by the storm's actual heading and provides a consistent reference frame for all subsequent composite analyses. In the vertical, every retained profile was linearly interpolated onto 56 common depth levels from the sea surface to 2000 m, yielding a uniform vertical grid across the entire dataset.

2.4 Archived dataset structure and usage guide

To facilitate direct use in studies of TC-induced ocean thermal and salinity responses, the final paired dataset was archived in six netCDF files. The files are separated by hemisphere (Northern Hemisphere and Southern Hemisphere) and by time period (2000–2009, 2010–2019, and 2020–2024). This file organization preserves the full global coverage of the dataset while keeping the size of each file manageable for download, reading, and subsequent analysis.

Each file is organized by paired record. A record represents one TC track point and its associated background-field and response-field Argo profiles. The archived variables include TC metadata, profile identifiers, observation times, geographic locations, storm-relative positions, relative sampling times, and the vertically gridded temperature and salinity fields. The anomaly variables, *Temp_dif* and *Salt_dif*, are defined as the response-field profile minus the corresponding background-field profile. Thus, negative temperature anomalies indicate TC-induced cooling, whereas positive salinity anomalies indicate response-field salinification.

https://doi.org/10.5194/essd-2026-520
Preprint. Discussion started: 27 July 2026

Open Access Earth System Science Data Discussions

Because the quality control, TC–Argo pairing, coordinate transformation, and vertical interpolation have already been applied as described in Sects. 2.2 and 2.3, users can directly subset the files by hemisphere, basin, storm intensity, relative time, storm-relative position, or depth for composite and statistical analyses. Detailed variable names, units, dimensions, and descriptions are provided in Table S5 of the Supplementary Material. In particular, users who require a more conservative definition of the TC-affected region can apply additional spatial or vertical constraints using the archived *X, Y*, and *Depth* variables. For example, analyses focused on the inner cold wake may be restricted to profiles within a few hundred kilometers of the track and to the upper ocean, whereas studies of broader upper-ocean adjustment or background variability may retain a larger spatial domain or deeper layers. We therefore recommend that users choose the spatial and vertical subsets according to the scientific question being addressed, rather than treating the 1000 km archive limit as a universal analysis radius.

3 Technical validation

3.1 Overview of the dataset

Because the pairing window spans from 10 d before tropical cyclone passage to 35 d after TC passage, original Argo files from January 1999 to February 2025 were examined to ensure complete coverage of TC events during 2000–2024. In total, 2910954 original Argo files were screened. After applying the pairing method and the strict quality control procedures described in Sect. 2, 3164876 high-quality paired Argo profiles were retained, including 2747731 pairs in the Northern Hemisphere and 417145 pairs in the Southern Hemisphere (Table 1; Fig. 2).

As the global Argo observing system expanded and the number of floats increased, the coverage of TCs by paired Argo profiles rose markedly. The annual ratio of TCs with paired Argo profiles to the total number of TCs increased from only 2.65% in 2000 to 95%–100% in recent years (Figure 3, Tables S1 and S2). This broad and stable coverage provides a robust observational basis for analyses of TC-induced ocean thermal and salinity responses, as well as related multiscale physical ocean processes. Furthermore, as shown in Figure 3, Tables S3 and S4, the monthly distribution of paired Argo profiles exhibits a clear seasonal cycle. In the Northern Hemisphere, more paired profiles are found in boreal summer and autumn, whereas in the Southern Hemisphere they are concentrated mainly in boreal winter to spring,

https://doi.org/10.5194/essd-2026-520
Preprint. Discussion started: 27 July 2026

corresponding to austral summer to autumn. This pattern is consistent with the seasonal cycle of tropical cyclone activity, because TC genesis is generally favored over warm ocean surfaces and is classically associated with sea surface temperatures above about 26.5 °C (Gray, 1968; McTaggart-Cowan et al., 2015). The monthly variability of the paired sample therefore largely mirrors the hemispheric contrast in seasonal TC activity.

Table 1. Number of Argo profile pairs archived in each netCDF file

Time band (years)	Northern hemisphere	Southern hemisphere
2000–2009	240262	54863
2010–2019	1873517	257599
2020–2024	633952	104683
Total	2747731	417145
	3164876	

The spatial distribution of TC track points and paired Argo profiles (Fig. 2) reveals significant hemispheric and basin-scale heterogeneity. While Fig. 2a shows all global TC tracks (2000–2024) from IBTrACS, Fig. 2b specifically highlights the Argo profiles that met our rigorous pairing and quality control criteria. At the hemispheric scale, paired samples are predominantly concentrated in the Northern Hemisphere (NH). This pattern aligns with the climatological distribution of TC activity; historical records indicate that approximately two-thirds of global TCs occur in the NH (Knapp et al., 2010; Wang et al., 2019). Furthermore, the NH benefits from a more mature and denser Argo array, particularly in the North Pacific and North Atlantic, whereas the Southern Ocean remains relatively under-sampled (Riser et al., 2016). Consequently, the synergy of higher storm frequency and superior observational density leads to a larger sample size in the NH (Fig. 3b, c).

On a basin scale, the western North Pacific exhibits the highest density of both TC tracks and paired Argo profiles. As the world's most prolific TC basin, it accounts for nearly one-third of global annual genesis (Maue, 2011). The abundance of data in this region reflects both the intense natural storm activity and the robust deployment of Argo floats in the tropical and subtropical Pacific (Roemmich et al., 2019).

https://doi.org/10.5194/essd-2026-520
Preprint. Discussion started: 27 July 2026

Overall, the dataset's distribution is a joint product of TC climatology and the evolving spatial coverage of the Argo program.

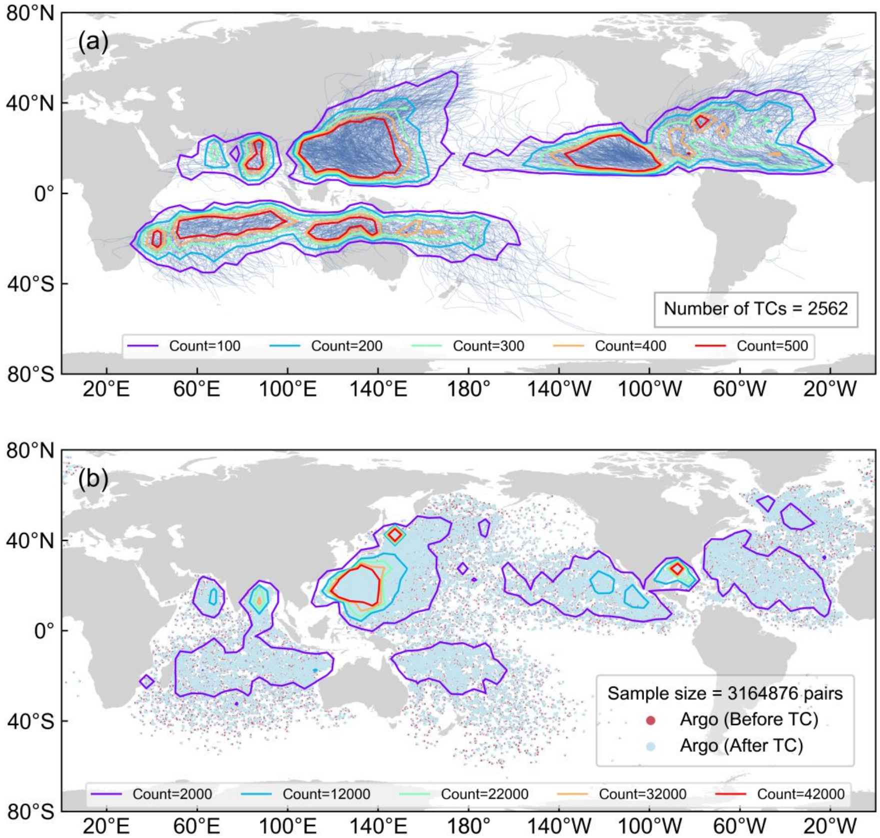

Figure 2. Spatial distribution of (a) global tropical cyclone track points and (b) Argo profile pairs associated with tropical cyclones within 1000 km during 2000–2024. In panel (a), the contours represent TC track-point density. In panel (b), the contours represent Argo profile density, with red points indicating background-field Argo locations and blue points indicating response-field Argo locations.

https://doi.org/10.5194/essd-2026-520
Preprint. Discussion started: 27 July 2026

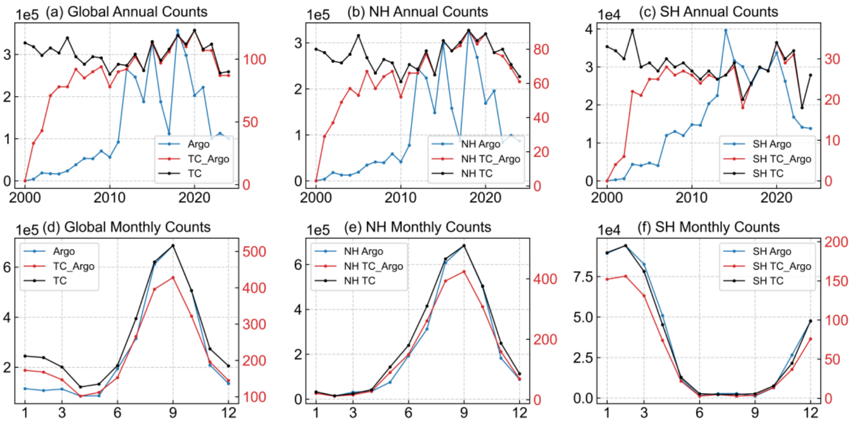

Figure 3. Annual and monthly variations in the counts of Argo pairs, total TC, and tropical cyclones associated with Argo pairs (TC_Argo) for the globe, Northern Hemisphere (NH), and Southern Hemisphere (SH). Panels (a)–(c) present the annual counts for the globe, NH, and SH, respectively, while panels (d)–(f) present the corresponding monthly counts. Here, Argo represents the number of Argo pairs, TC_Argo represents the number of tropical cyclones with matched Argo pair observations, and TC represents the total number of tropical cyclones.

Figure 4 shows the spatial distribution of paired Argo records in the six archived netCDF files in the TC-relative coordinate system defined by *X_argo_re* and *Y_argo_re*. In this system, the TC center is set as the origin and the TC translation direction is aligned with the positive Y axis. Because the distance between the background-field and response-field Argo locations in each pair is less than 50 km, only the response-field Argo positions are plotted, but they can represent the distribution of the full paired dataset. All samples are located within 1000 km of the TC center, indicating that the coordinate transformation is consistent with the pairing radius used in this study. The overall pattern is consistent with Figures 2 and 3, with substantially more paired Argo records in the NH than in the SH. Among the six files, the two files covering 2010–2019 contain the largest number of records, reflecting both the longer 10-year period and the rapid expansion of the global Argo observing system during this stage.

https://doi.org/10.5194/essd-2026-520
Preprint. Discussion started: 27 July 2026

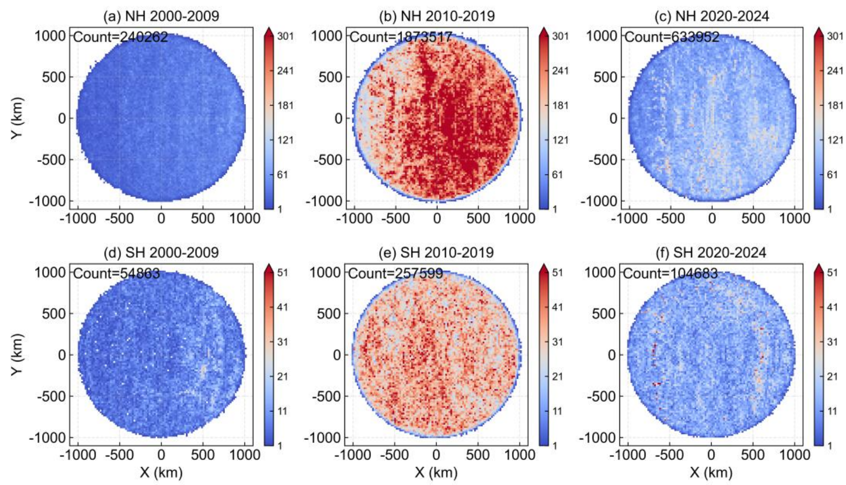

Figure 4. Spatial distribution of paired Argo records archived in the six netCDF files in the TC-relative coordinate system. The coordinates are given by the variables *X_argo_re* and *Y_argo_re*, in which the TC center is set as the origin and the TC translation direction is aligned with the positive Y axis. Panels (a–c) show the distributions for the three Northern Hemisphere netCDF files, and panels (d–f) show those for the three Southern Hemisphere netCDF files. Because the distance between the background-field and response-field Argo profile locations in each pair is less than 50 km, only the response-field Argo locations are plotted to represent the spatial distribution of the full paired Argo dataset.

3.2 Spatial validation of the archived dataset

To assess whether the archived dataset faithfully captures the canonical upper-ocean response to TCs, and to verify the usability and correctness of the variables, we conducted validations using three complementary approaches. In the Supplementary Material, we present anomalies calculated manually by subtracting the undisturbed background field (averaged over the -10 to -4 d background window, using *Temp_ba* and *Salt_ba*) from the response-field observations (*Temp_re* and *Salt_re*). These manually derived results (e.g., Figs. S1, S4, S6, and S8) exhibit negligible differences from the composites generated directly using the precomputed anomaly variables (*Temp_dif* and *Salt_dif*) archived in the dataset (Figs. S3, S5, and S7). This consistency shows the correctness of the dataset variables. We also compared the Argo-based surface composites with independent sea surface temperature fields from

https://doi.org/10.5194/essd-2026-520
Preprint. Discussion started: 27 July 2026

Remote Sensing Systems (REMSS) and salinity fields from the Copernicus Marine Service product cmems_mod_glo_phy_my_0.083deg_P1D-m; the broadly consistent surface cooling and salinity-response patterns provide additional support for the reliability and usability of the archived Argo dataset (Fig. S2). Consequently, to maintain conciseness, the analyses presented in the main text exclusively utilize the precomputed "*_dif*" variables. Detailed cross-validations utilizing the independently computed "*_ba*" and "*_re*" variables are provided in the Supplementary Material and are not reiterated in the main text.

Following this, we selected samples with *Relative_time_re* ∈ [0, 7] d, and directly composited them in the storm-relative coordinate system defined by *X_argo_re* and *Y_argo_re* (Fig. 5). Although the archived dataset retains records out to 1000 km from the TC center, the validation analyses below use the storm-relative coordinates to focus on narrower domains that are most relevant to the upper-ocean response, such as profiles close to the storm track for the vertical sections and within ±300 km for the cross-track temporal composites. In this framework, the TC center is set as the origin and the translation direction is aligned with the positive Y axis. This approach allows Fig. 5 to focus specifically on the early upper-ocean response within 0–7 days after TC passage. The sea surface temperature (SST) composites show clear negative anomalies near and behind the storm center in both hemispheres, indicating robust TC-induced surface cooling (Fig. 5a, b). A distinct hemispheric asymmetry is also evident: cooling is stronger on the right-hand side of the track in the Northern Hemisphere, where the maximum cooling reaches -4.55 °C, but on the left-hand side in the Southern Hemisphere, where the maximum cooling reaches -4.59 °C. This pattern is consistent with the well-established asymmetric upper-ocean response to TC wind forcing, in which the resonance between rotating wind stress and near-inertial currents, together with stronger effective wind forcing on the right (left) side of the storm track in the Northern (Southern) Hemisphere, enhances vertical mixing and entrainment there (Price, 1981; D'Asaro et al., 2007; D'Asaro et al., 2014; Mei and Pasquero, 2013). The SST structure in Fig. 5 therefore reproduces the canonical thermal signature of TC-ocean interaction and supports the physical reliability of the archived dataset. Radius-threshold sensitivity tests using 300, 500, and 1000 km domains show that the main composite SST pattern and peak cooling are stable, indicating that the radial threshold has little effect on the composite conclusions (Table S6).

https://doi.org/10.5194/essd-2026-520
Preprint. Discussion started: 27 July 2026

In contrast, the sea surface salinity (SSS) composites are weaker and less spatially coherent than their SST counterparts (Fig. 5c, d). After TC passage, SSS in the Northern Hemisphere can increase by up to 0.62 PSU or decrease by up to 0.75 PSU. Meanwhile, in the Southern Hemisphere, SSS can increase by up to 0.84 PSU or decrease by up to 0.54 PSU. This feature is more likely a reflection of the intrinsic complexity of salinity response than a simple limitation of the dataset. Unlike SST, whose response is largely controlled by entrainment cooling and therefore tends to exhibit a relatively stable sign and structure (D'Asaro et al., 2007; He et al., 2023; Wang et al., 2024; Wang and Xiu, 2022; Mei and Pasquero, 2013), the SSS response reflects the combined effects of rainfall freshening, evaporation, vertical mixing, upwelling of subsurface water, and horizontal advection of surrounding water masses (Liu et al., 2007; Fu et al., 2014; Reul et al., 2021). For example, recent observations and numerical experiments over the Changjiang River Plume showed that TC-induced vertical mixing can consistently increase surface salinity, whereas horizontal advection may either enhance or offset salinification depending on local salinity gradients and surface currents (Guan et al., 2025). As a result, TC-induced surface salinity anomalies are much more sensitive to regional hydrography, background salinity stratification, river-plume influence, and the stage of response evolution (Qiu et al., 2019; Zhang et al., 2021; Jourdain et al., 2013). Previous studies have shown that the sea surface often freshens during or shortly after TC passage because of heavy rainfall, but this signal may later be offset or even reversed when vertical mixing and upwelling bring saltier subsurface water upward (Reul et al., 2021; Sun et al., 2021a). Because of this competition among processes and its strong phase dependence, the SSS response is inherently less uniform than the SST response, even within the 0–7 day period considered here. In other words, the relatively diffuse SSS pattern in Fig. 5 does not imply that the dataset fails to capture salinity variability; rather, it suggests that TC-induced surface salinity changes are intrinsically less stable and less spatially consistent than temperature changes.

https://doi.org/10.5194/essd-2026-520
Preprint. Discussion started: 27 July 2026

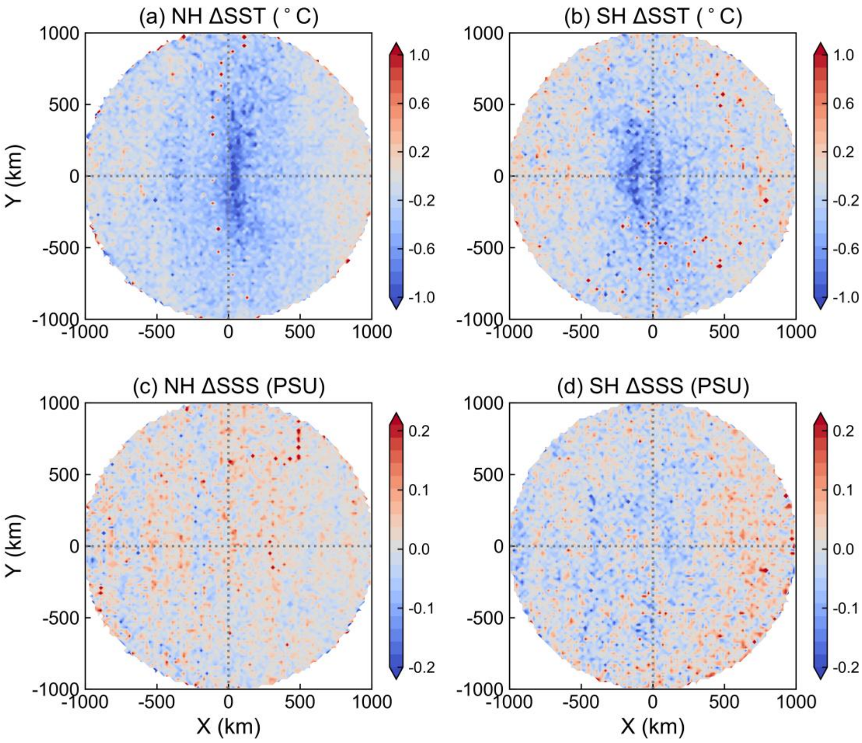

Figure 5. Composite distributions of TC-induced sea surface temperature (SST) and sea surface salinity (SSS) anomalies derived from the archived netCDF dataset. Panels (a) and (b) show SST anomalies (°C) in the Northern Hemisphere and Southern Hemisphere, respectively, and panels (c) and (d) show SSS anomalies (PSU) for the corresponding hemispheres. The anomalies are directly obtained from the precomputed variables *Temp_dif* and *Salt_dif* in the netCDF files, defined as response field minus background field values. The distributions are presented in the TC-relative coordinate system, where the TC center is set as the origin and the translation direction is aligned with the positive Y axis.

Figures 6, 7, S3, and S5 were composited directly using the *Temp_dif*, *Salt_dif*, and Depth variables from the archived Argo dataset. The results shown were obtained by directly averaging the temperature and salinity profiles within 100 km of the corresponding tracks based on *X_argo_re* and *Y_argo_re*. The results indicate that the dominant temperature response following a TC passage remains concentrated in the upper ocean. The clearest negative temperature anomalies are primarily confined to the upper 200 m

https://doi.org/10.5194/essd-2026-520
Preprint. Discussion started: 27 July 2026

below the sea surface, and are most pronounced near the TC center and its adjacent track region. Specifically, in the along-track direction, negative temperature anomalies reach -0.82 °C in the Northern Hemisphere and -0.69 °C in the Southern Hemisphere (Fig. 6a, b). In the cross-track direction, these anomalies reach -1.13 °C in the Northern Hemisphere and -0.84 °C in the Southern Hemisphere (Fig. 7a, b). The along-track profiles show that upper-ocean cooling is the most robust common signal, while a weaker compensatory warm anomaly is visible in the subsurface (Fig. 6a, b). Furthermore, the cross-track profiles reveal a distinct mirror-image asymmetry in the temperature responses between the two hemispheres; that is, the strongest cooling is located on opposite sides of the track (Fig. 7a, b). This structure is consistent with previous findings based on Argo composites, mooring observations, and case studies: TC passage typically results in the coexistence of surface cooling, subsurface warming, or deeper upwelling-induced cooling, with the responses biased toward opposite sides in the two hemispheres (Cheng et al., 2015; Zhang et al., 2016; Zhang, 2023; Han et al., 2024, 2025).

Furthermore, the composited salinity signal is notably weaker than the temperature signal and more frequently exhibits an out-of-phase vertical structure, characterized by opposite signs between the surface and subsurface. This is a typical manifestation of the salinity response to TCs being more complex than the temperature response. After TC passage, within the upper 200 m, the maximum salinity anomalies reach +0.16 PSU and -0.07 PSU in the Northern Hemisphere (Figs. 6c, 7c). Meanwhile, in the Southern Hemisphere, the maximum salinity anomalies reach +0.07 PSU and -0.09 PSU (Figs. 6d, 7d). This occurs because salinity changes are jointly controlled by precipitation-induced freshening, vertical mixing, upwelling, and background salinity stratification (Sala et al., 2024). Consequently, the composited salinity signals are generally less continuous and coherent than the temperature signals. Figures S3 and S5 in the Supplementary Material further demonstrate that extending the analysis depth from 1000 m to 2000 m does not alter the primary conclusions. The most coherent salinity anomalies remain concentrated in the upper ocean, whereas signals below 1000 m weaken significantly and become scattered. This is consistent with existing studies suggesting that while deep-ocean responses can occur, they are typically weaker and more localized (Steffen and Bourassa, 2018; Qiu et al., 2019; Sala et al., 2024; Zhang et al., 2022; Han et al., 2025). This agreement further supports the physical reliability of this data product. Additionally, both temperature and salinity profiles exhibit discrete columnar extrema within the 1000–

https://doi.org/10.5194/essd-2026-520
Preprint. Discussion started: 27 July 2026

2000 m depth range (Figs. S3, S5). This may be due to the spatial overlap of the primary upwelling peaks of different baroclinic modes following TC passage; such multimodal phase alignment induces a vertical columnar upwelling structure (Furue et al., 2024; Zhang et al., 2022). Overall, the downward propagation of TC-generated near-inertial internal waves, the columnar vertical responses triggered by inertial pumping, and enhanced near-bottom turbulent mixing collectively contribute to the formation of these discrete, strong anomalous signals in the 1000–2000 m deep layer (Furue et al., 2024; Zhang et al., 2024c; van Haren et al., 2020).

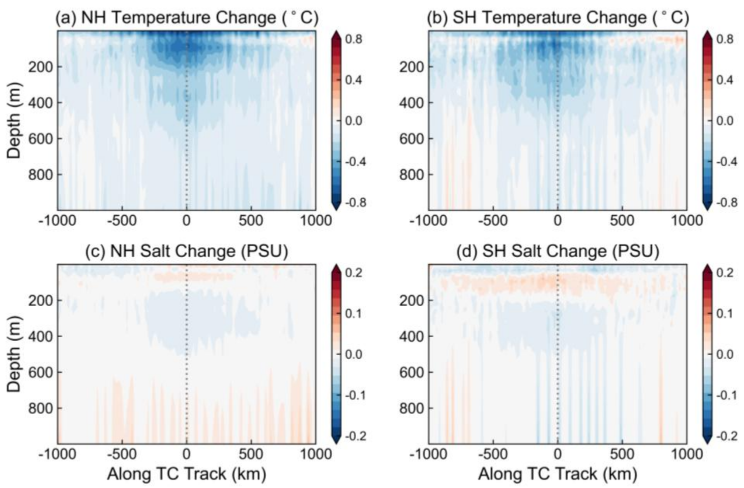

Figure 6. Composite depth–distance sections of TC-induced temperature and salinity anomalies along the TC track in the Northern Hemisphere and Southern Hemisphere. Panels (a) and (c) show temperature and salinity anomalies in the Northern Hemisphere, respectively, and panels (b) and (d) show the corresponding anomalies in the Southern Hemisphere. The anomalies are directly obtained from the precomputed variables *Temp_dif* and *Salt_dif* in the netCDF files, defined as response field minus background field values. The y axis denotes depth from 0 to 1000 m, and the x axis denotes along-track distance relative to the TC center (km), with positive values indicating the region ahead of the TC and negative values indicating the region behind the TC.

https://doi.org/10.5194/essd-2026-520
Preprint. Discussion started: 27 July 2026

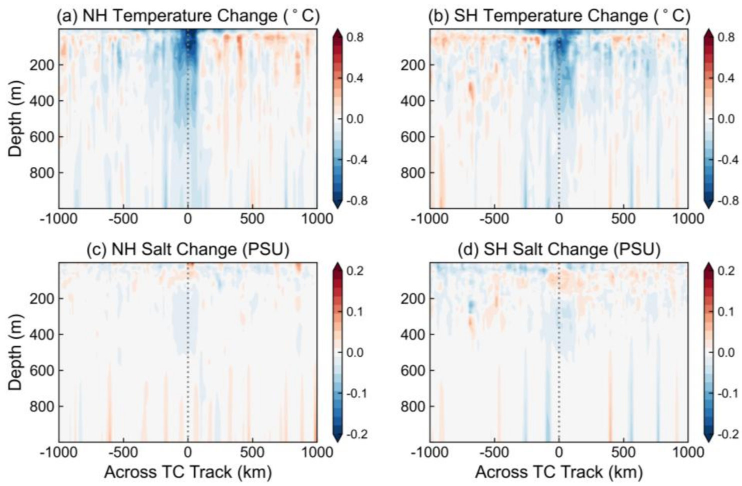

Figure 7. Same as Fig. 6, but for composite sections in the cross-track direction relative to the TC track; negative and positive distances denote the left and right sides of the track, respectively.

3.3 Temporal validation of the archived dataset

Figure 8 evaluates the capability of the archived dataset to capture the temporal evolution of tropical cyclone-induced ocean responses. In both hemispheres, temperature anomalies remain generally close to zero prior to TC passage, confirming that the [-10, -4] day background-field matching window used in this study stably reflects the undisturbed ocean background state. Following TC passage, significant cooling rapidly emerges in the upper ocean of both hemispheres; this cooling signal is primarily concentrated within the upper 200 m of the water column and exhibits a gradual weakening recovery trend over the subsequent month. This temporal evolution is consistent with the canonical paradigm wherein vertical confinement, wind stress-driven near-inertial shear entrainment, and vertical mixing act as the dominant mechanisms (Price, 1981; D'Asaro et al., 2007; Zhang et al., 2021). Further comparison with Fig. S7, which extends the depth range to 0–2000 m, reveals that the primary temperature response features identified in Fig. 8 remain robust, meaning the significant anomalies are still mainly concentrated within the upper ~200 m. In comparison, only scattered and intermittent weak anomalous signals appear in the 1000–2000 m depth range, indicating that while deep-ocean responses exist, their continuity and overall contribution are markedly weaker than those in the upper ocean. Furthermore, the salinity anomalies are weaker in both magnitude and temporal continuity than the temperature anomalies,

https://doi.org/10.5194/essd-2026-520
Preprint. Discussion started: 27 July 2026

and opposite signs can appear between the surface and subsurface layers. This pattern reflects that the TC-induced ocean salinity budget is not governed by a single process, but is rather a combined response to precipitation-induced freshening, vertical mixing, upwelling, and background salinity stratification (Fu et al., 2014; Reul et al., 2021; Sun et al., 2021a). The temporal evolution and vertical structural features presented in Fig. 8 mutually corroborate the spatial composite results in Figs. 5 to 7, further supporting the physical reliability of this dataset in characterizing TC-induced upper-ocean temperature and salinity responses at the global scale.

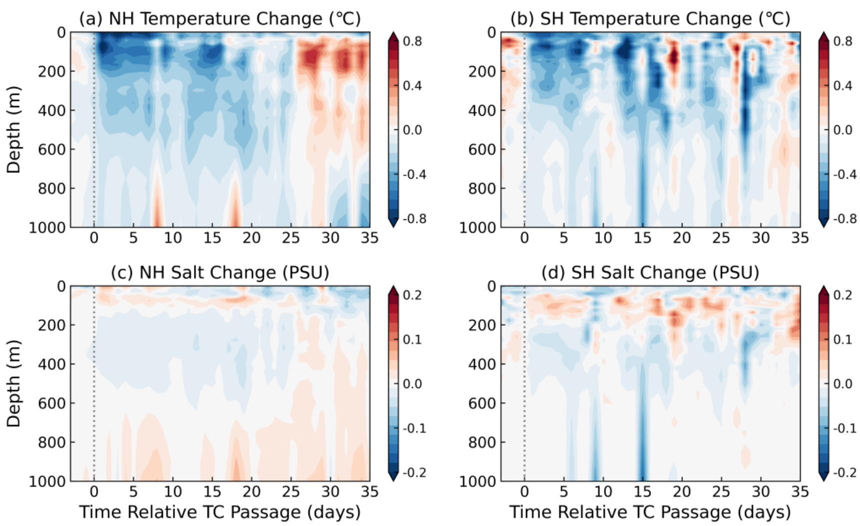

Figure 8. Temporal evolution of TC-induced temperature and salinity anomalies within 0–1000 m from 3 days before to 35 days after tropical cyclone passage in the Northern Hemisphere and Southern Hemisphere. Panels (a) and (b) show temperature anomalies (°C) in the Northern Hemisphere and Southern Hemisphere, respectively, and panels (c) and (d) show the corresponding salinity anomalies (PSU). The anomalies are directly obtained from the precomputed variables *Temp_dif* and *Salt_dif* in the netCDF files, defined as response field minus background field values. The vertical dashed line marks the time of TC passage.

Figure 9 illustrates the joint spatio-temporal evolution of TC-induced SST and SSS anomalies in the cross-track–time plane from 3 days before to 35 days after TC passage. This surface evolution is also

https://doi.org/10.5194/essd-2026-520
Preprint. Discussion started: 27 July 2026

consistent with recent drifter-based evidence that storm-local cooling should be evaluated with in situ observations because satellite-based cold-wake estimates may overestimate inner-core cooling under storm conditions (Guan et al., 2026). SST cooling exhibits a pronounced temporal lag in both hemispheres: the maximum cooling in the Northern Hemisphere (approximately -1.02 °C) occurs roughly 2.5 days after TC passage at ~30 km to the right of the track, while the Southern Hemisphere peak (approximately -0.90 °C) is reached at a comparable post-passage lag but is displaced ~130 km to the left of the track. This ~2–3 day peak lag is highly consistent with the SST response timescales revealed by satellite and in situ observations, reflecting the finite time required for near-inertial wind shear-driven turbulent mixing to sufficiently erode the thermocline and fully cool the surface (Dare and McBride, 2011; Vincent et al., 2012a; Wang et al., 2026a; Wang and Xiu, 2022). The cross-track asymmetry—with the cooling signal biased toward the right (left) of the track in the Northern (Southern) Hemisphere—is a classic manifestation of Coriolis-modulated resonance between the rotating wind stress and near-inertial currents, which amplifies vertical mixing on the stronger-forcing side (Gill, 1984; Price, 1981; Ma et al., 2023).

Subsequently, the cold SST anomalies gradually attenuate over approximately 1–2 weeks following TC passage, consistent with upper-ocean heat re-injection and re-stratification (Vincent et al., 2012b). Notably, following this recovery phase, a distinct anomalous warming (positive SST anomalies > 1.0 °C, visible as the prominent red patch in Fig. 9a) emerges in the Northern Hemisphere roughly 15 to 30 days post-passage. This post-cyclone “warming overshoot” is primarily driven by the rapid solar heating of a newly formed, shallow, re-stratified surface mixed layer under clear-sky conditions during recovery (Price et al., 2008; Mei and Pasquero, 2013; Pasquero and Emanuel, 2008; Pasquero et al., 2021). Furthermore, as indicated by the corresponding delayed freshening (negative SSS anomalies) in Fig. 9c, the enhanced salinity stratification effectively traps the incoming shortwave radiation within a thinner surface layer, further amplifying the warming signal (Balaguru et al., 2012; Reul et al., 2014). In contrast, the overall SSS response is notably weaker and spatially more diffuse: the Northern Hemisphere displays a maximum salinification of ~0.13 PSU at ~30 km to the right of the track and ~1.5 days post-passage, whereas the Southern Hemisphere exhibits only ~0.026 PSU at ~150 km to the left of the track and ~4.5 days post-passage. The cross-track positions of peak salinification broadly coincide with those of

https://doi.org/10.5194/essd-2026-520
Preprint. Discussion started: 27 July 2026

maximum SST cooling in both hemispheres, suggesting a shared vertical-mixing-dominated driving mechanism. Nevertheless, the SSS response is systematically weaker, more delayed, and exhibits greater hemispheric contrast. This reflects the complex competing effects among precipitation-induced freshening, upwelling, and background salinity stratification (Reul et al., 2021; Jourdain et al., 2013), as well as the distinct freshwater forcing environments between the two hemispheres.

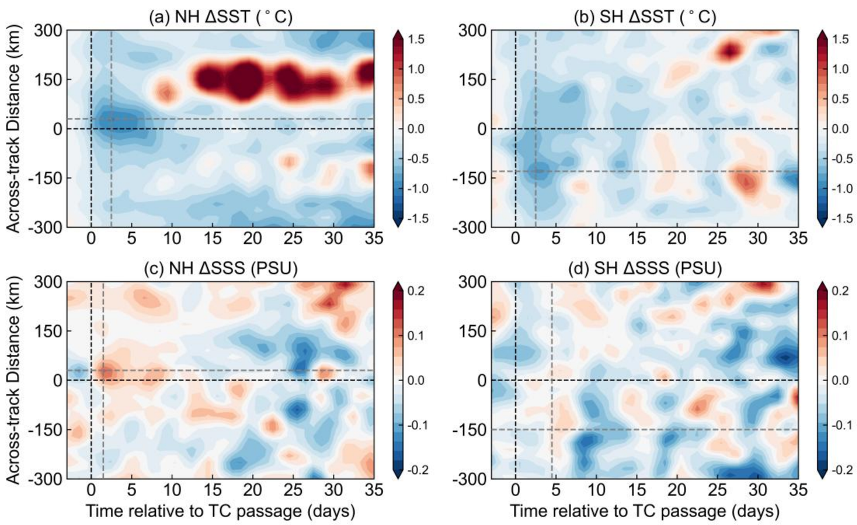

Figure 9. Spatio-temporal evolution of TC-induced SST and SSS anomalies in the cross-track–time plane from 3 days before to 35 days after TC passage. Panels (a) and (b) show SST anomalies (°C) within ±300 km of the TC track for the Northern and Southern Hemispheres, respectively; panels (c) and (d) show the corresponding SSS anomalies (PSU). The horizontal black dashed line marks the TC track center (zero cross-track distance), with negative (positive) values denoting distances to the left (right) of the track. The vertical black dashed line marks the time of TC passage (day 0). The gray horizontal and vertical dashed lines indicate the cross-track position and the number of days after TC passage at which the maximum surface response occurs, respectively.

4 Conclusions

This paper presents a global paired Argo dataset for ocean thermal and salinity responses to tropical cyclones (TCs) from 2000 to 2024, built by combining the IBTrACS best-track data with the Global

https://doi.org/10.5194/essd-2026-520
Preprint. Discussion started: 27 July 2026

Ocean Argo Scatter Dataset (V3.0) from the China Argo Real-time Data Center. The construction followed a strict screening workflow. On top of the original quality-control flags, we applied a secondary check and discarded any profile in which the flag was not equal to 1 at any vertical level or which contained invalid values, and we further required the deepest observation to reach at least 1900 m. A 1000 km search radius around the TC center was then used to identify candidate floats, with background-field and response-field matching windows of -10 to -4 days and -3 to +35 days relative to TC passage, and with the background-field and response-field observation sites constrained to within 50 km of each other. All retained profiles were interpolated onto 56 standard levels from the surface to 2000 m and rotated into a TC-relative coordinate system in which the TC center is the origin and the translation direction aligns with the positive Y axis. The final dataset contains 3,164,876 paired records (2,747,731 in the Northern Hemisphere and 417,145 in the Southern Hemisphere) and is archived as six netCDF files, split by hemisphere and by period (2000–2009, 2010–2019, and 2020–2024), so that the full global coverage is preserved while each file remains easy to download and handle. Every record provides the basic TC information, the IDs, times and locations of both paired Argo profiles, the along- and cross-track distances, the relative times, the background-field and response-field temperature and salinity profiles, and the precomputed anomalies (response field minus background field). Users can therefore move directly to composite and statistical analyses without having to repeat the download, quality control, pairing, or interpolation themselves.

Validation in the spatial, vertical and temporal dimensions shows that the dataset reproduces the canonical features of the TC-forced upper-ocean response. The cross-track cooling is biased to the right of the track in the Northern Hemisphere and to the left in the Southern Hemisphere, forming a clear hemispheric mirror image. The strongest thermal response is concentrated within the upper ~200 m, while signals below 1000 m are scattered and much weaker. Peak SST cooling appears about 2.5 days after TC passage and decays over the following 1–2 weeks, and a distinct response-period warming overshoot emerges 15–30 days after passage in the Northern Hemisphere. The salinity response is weaker and less continuous in both space and time than the temperature response, reflecting the competing effects of rainfall freshening, vertical mixing, upwelling, and background stratification. These results agree closely with previous observational, modeling, and theoretical studies, which supports the physical

https://doi.org/10.5194/essd-2026-520
Preprint. Discussion started: 27 July 2026

Open Access Earth System Science Data Discussions

reliability of the product. By providing analysis-ready paired records at global scale, this dataset considerably reduces the time researchers have to spend on screening, spatiotemporal matching, and preprocessing of in situ Argo observations, and offers a ready-to-use observational benchmark for studies of TC–ocean interaction, upper-ocean heat and salt budgets, mixed-layer and near-inertial responses, and the evaluation of coupled ocean–atmosphere models.

Code and data availability

The paired Argo dataset and associated data-generation code described in this paper are openly archived on Figshare at https://doi.org/10.6084/m9.figshare.32820563 (Wang et al., 2026b). The dataset is distributed as six netCDF files following the naming convention north_Argo_tc_pairing_2000_2009_(2000m)_QC and south_Argo_tc_pairing_2000_2009_(2000m)_QC, as described in Sect. 2.4. The IBTrACS best-track data are available from NOAA NCEI at https://www.ncei.noaa.gov/products/international-best-track-archive (Knapp et al., 2010; Gahtan et al., 2024). The Global Ocean Argo Scatter Dataset (Version 3.0) is provided by the China Argo Real-time Data Center at https://www.argo.org.cn/index.php?m=content&c=index&a=lists&catid=27 (last access: 25 July 2026) (Argo data management, 2025). The SST data used for validation were obtained from the REMSS daily MW_IR SST product at https://data.remss.com/SST/daily/mw_ir/v05.1/netcdf (Gentemann et al., 2003; Gentemann et al., 2004; Gentemann et al., 2010; Wentz et al., 2000). The salinity data used for validation were obtained from the Copernicus Marine GLORYS12V1 product at https://data.marine.copernicus.eu/product/GLOBAL_MULTIYEAR_PHY_001_030/download?dataset=cmems_mod_glo_phy_my_0.083deg_P1D-m_202311 (Lellouche et al., 2021).

Author contribution

XW created the dataset and wrote the whole manuscript. The whole observation project was designed by HZ and TL. The flow of the manuscript was revised by MX, JL, and DT, and the dataset was optimized by MX, HZ, TL, and JY.

Competing interests

The authors declare that they have no conflict of interest.

Acknowledgements

We thank all scientists, engineers, technicians, data managers, and institutions who have contributed to the development, operation, quality control, and data distribution of the global Argo program.

Financial support

This research was funded by the Zhejiang Provincial Natural Science Foundation of China (LR26D060001), the National Natural Science Foundation of China (42530402), the Scientific Research Fund of the Second Institute of Oceanography, MNR (SOEDZZ2506), the Project of State Key Laboratory of Satellite Ocean Environment Dynamics (SOEDZZ2532), the Key R&D Program of Zhejiang Province (2024C03257), the National Key Research and Development Program of China (2023YFF0805300, 2023YFF0805301), the National Natural Science Foundation of China (42227901), the project from the Shanghai Frontiers Science Center of Atmosphere-Ocean Interaction, Fudan University, Shanghai, China (FDAOS-OP202301), the Innovation Group Project of Southern Marine Science and Engineering Guangdong Laboratory (Zhuhai) (311024001), the Project supported by Southern Marine Science and Engineering Guangdong Laboratory (Zhuhai) (SML2021SP207, SML2024SP012).

References

Aberson, S. D., Black, M. L., Black, R. A., Burpee, R. W., Cione, J. J., Landsea, C. W., and Marks Jr, F. D.: Thirty years of tropical cyclone research with the NOAA P-3 aircraft, Bull. Am. Meteorol. Soc., 87, 1039-1056, https://doi.org/10.1175/BAMS-87-8-1039, 2006.

Argo data management: Argo user's manual, Ifremer, https://doi.org/10.13155/29825, 2025.

Balaguru, K., Chang, P., Saravanan, R., Leung, L. R., Xu, Z., Li, M., and Hsieh, J. S.: Ocean barrier layers' effect on tropical cyclone intensification, P. Natl. Acad. Sci. USA, 109, 14343-14347, https://doi.org/10.1073/pnas.1201364109, 2012.

Cheng, L., Zhu, J., and Sriver, R. L.: Global representation of tropical cyclone-induced short-term ocean thermal changes using Argo data, Ocean Sci., 11, 719-741, https://doi.org/10.5194/os-11-719-2015, 2015.

https://doi.org/10.5194/essd-2026-520
Preprint. Discussion started: 27 July 2026

D'Asaro, E., Sanford, T. B., Niiler, P. P., and Terrill, E. J.: Cold wake of hurricane Frances, Geophys. Res. Lett., 34, L15609, https://doi.org/10.1029/2007GL030160, 2007.

D'Asaro, E., Black, P., Centurioni, L., Chang, Y.-T., Chen, S., Foster, R., Graber, H., Harr, P., Hormann, V., and Lien, R.-C.: Impact of typhoons on the ocean in the Pacific, Bull. Am. Meteorol. Soc., 95, 1405-1418, https://doi.org/10.1175/BAMS-D-12-00104.1, 2014.

Dare, R. A. and McBride, J. L.: Sea Surface Temperature Response to Tropical Cyclones, Mon. Weather Rev., 139, 3798-3808, https://doi.org/10.1175/mwr-d-10-05019.1, 2011.

DeMaria, M., Knaff, J. A., Sampson, C. R., Peak, J. E., Cummings, J., and Schubert, W. H.: Upper Oceanic Energy Response to Tropical Cyclone Passage, J. Clim., 26, 2631-2650, https://doi.org/10.1175/jcli-d-12-00038.1, 2013.

Domingues, R., Kuwano-Yoshida, A., Chardon-Maldonado, P., Todd, R. E., Halliwell, G., Kim, H.-S., Lin, I. I., Sato, K., Narazaki, T., Shay, L. K., Miles, T., Glenn, S., Zhang, J. A., Jayne, S. R., Centurioni, L., Le Hénaff, M., Foltz, G. R., Bringas, F., Ali, M. M., DiMarco, S. F., Hosoda, S., Fukuoka, T., LaCour, B., Mehra, A., Sanabia, E. R., Gyakum, J. R., Dong, J., Knaff, J. A., and Goni, G.: Ocean Observations in Support of Studies and Forecasts of Tropical and Extratropical Cyclones, Front. Mar. Sci., 6, 446, https://doi.org/10.3389/fmars.2019.00446, 2019.

Falor, D., Gayen, B., Sengupta, D., and Chaudhuri, D.: Enhanced Ocean Mixing During the Passage of Tropical Cyclone, Geophys. Res. Lett., 51, https://doi.org/10.1029/2024gl111925, 2024.

Fu, H., Wang, X., Chu, P. C., Zhang, X., Han, G., and Li, W.: Tropical cyclone footprint in the ocean mixed layer observed by Argo in the Northwest Pacific, J. Geophys. Res.-Oceans, 119, 8078-8092, https://doi.org/10.1002/2014JC010316, 2014.

Furue, R., Fukao, Y., and Sugioka, H.: Linear response of deep ocean to a moving tropical cyclone, PLOS Clim., 3, e0000376, https://doi.org/10.1371/journal.pclm.0000376, 2024.

Gahtan, J., Knapp, K. R., Schreck, C. J. I., Diamond, H. J., Kossin, J. P., and Kruk, M. C.: International Best Track Archive for Climate Stewardship (IBTrACS) Project, Version 4.01 [dataset], https://doi.org/10.25921/82ty-9e16, 2024.

Gentemann, C. L., Donlon, C. J., Stuart-Menteth, A., and Wentz, F. J.: Diurnal signals in satellite sea surface temperature measurements, Geophys. Res. Lett., 30, https://doi.org/10.1029/2002gl016291, 2003.

Gentemann, C. L., Wentz, F. J., Mears, C. A., and Smith, D. K.: In situ validation of Tropical Rainfall Measuring Mission microwave sea surface temperatures, J. Geophys. Res.-Oceans, 109, https://doi.org/10.1029/2003jc002092, 2004.

Gentemann, C. L., Meissner, T., and Wentz, F. J.: Accuracy of Satellite Sea Surface Temperatures at 7 and 11 GHz, IEEE Trans. Geosci. Remote Sens., 48, 1009-1018, https://doi.org/10.1109/tgrs.2009.2030322, 2010.

Gill, A. E.: On the Behavior of Internal Waves in the Wakes of Storms, J. Phys. Oceanogr., 14, 1129-1151, https://doi.org/10.1175/1520-0485(1984)014<1129:OTBOIW>2.0.CO;2, 1984.

Gray, W. M.: Global view of the origin of tropical disturbances and storms, Mon. Weather Rev., 96, 669-700, https://doi.org/10.1175/1520-0493(1968)096%3C0669:GVOTOO%3E2.0.CO;2, 1968.

Guan, S., Huang, M., Lin, I. I., Wu, H., Lin, Y., Wu, Z., Zhang, Y., Jin, F.-F., Wang, W., Hong, X., Li, C., Liu, Z., Lin, X., Zhao, W., and Tian, J.: Widespread sea surface salinification induced by tropical cyclones over the Changjiang River Plume, Commun. Earth Environ., 6, 337,

https://doi.org/10.5194/essd-2026-520
Preprint. Discussion started: 27 July 2026

https://doi.org/10.1038/s43247-025-02317-x, 2025.

Guan, S., Huang, M., Cai, W., Zhang, Z., Lin, I. I., Kim, H.-S., Zhou, L., Lin, X., Xu, Z., Jin, F.-F., Mei, W., Wang, Q., Zhou, C., Meng, Z., Tian, J., and Zhao, W.: Weak self-induced cooling of tropical cyclones amid fast sea surface warming, Nat. Geosci., 19, 153-158, https://doi.org/10.1038/s41561-025-01879-x, 2026.

Han, C., Bowen, M., and Sutton, P.: The Response of the Upper Ocean to Tropical Cyclones in the South Pacific, J. Geophys. Res.-Oceans, 129, https://doi.org/10.1029/2023jc020627, 2024.

Han, C., Bowen, M., and Sutton, P.: Global Observations of the Response of the Upper Ocean to Tropical Cyclones Based on Argo Profiles, J. Geophys. Res.-Oceans, 130, https://doi.org/10.1029/2025jc022522, 2025.

Harper, B., Kepert, J., and Ginger, J.: Guidelines for converting between various wind averaging periods in tropical cyclone conditions, World Meteorological Organization, Geneva, Switzerland, 64 pp., 2010.

He, S., Cheng, X., Fei, J., Li, X., Wei, Z., and Huang, X.: Thermal response to sequential tropical cyclone passages: Statistic analysis and idealized experiments, Front. Earth Sci., 11, 1142537, https://doi.org/10.3389/feart.2023.1142537, 2023.

Hristova-Veleva, S. M., Li, P. P., Knosp, B., Vu, Q., Turk, F. J., Poulsen, W. L., Haddad, Z., Lambrigtsen, B., Stiles, B. W., and Shen, T.-P.: An eye on the storm: Integrating a wealth of data for quickly advancing the physical understanding and forecasting of tropical cyclones, Bull. Am. Meteorol. Soc., 101, E1718-E1742, https://doi.org/10.1175/BAMS-D-19-0020.1, 2020.

Hu, A. J., Kuusela, M., Lee, A. B., Giglio, D., and Wood, K. M.: Spatiotemporal methods for estimating subsurface ocean thermal response to tropical cyclones, Adv. Stat. Clim. Meteorol. Oceanogr., 10, 69-93, https://doi.org/10.5194/ascmo-10-69-2024, 2024.

Jacob, S. D., Shay, L. K., Mariano, A. J., and Black, P. G.: The 3D oceanic mixed layer response to Hurricane Gilbert, J. Phys. Oceanogr., 30, 1407-1429, https://doi.org/10.1175/1520-0485(2000)030<1407:TOMLRT>2.0.CO;2, 2000.

Jayne, S. R., Roemmich, D., Zilberman, N., Riser, S. C., Johnson, K. S., Johnson, G. C., and Piotrowicz, S. R.: The Argo Program Present and Future, Oceanography, 30, 18-28, https://doi.org/10.5670/oceanog.2017.213, 2017.

Jiang, Y., Wang, Y., Tian, X., Lin, S., Chen, S., Yu, J., and Chai, F.: Upper Ocean Structure Determines the Contrasting Typhoon-Induced Chlorophyll-a Responses in the Northwest Pacific, Geophys. Res. Lett., 50, e2023GL102930, https://doi.org/10.1029/2023gl102930, 2023.

Jourdain, N. C., Lengaigne, M., Vialard, J., Madec, G., Menkès, C. E., Vincent, E. M., Jullien, S., and Barnier, B.: Observation-based estimates of surface cooling inhibition by heavy rainfall under tropical cyclones, J. Phys. Oceanogr., 43, 205-221, https://doi.org/10.1175/JPO-D-12-085.1, 2013.

Knapp, K. R., Kruk, M. C., Levinson, D. H., Diamond, H. J., and Neumann, C. J.: The International Best Track Archive for Climate Stewardship (IBTrACS), Bull. Am. Meteorol. Soc., 91, 363-376, https://doi.org/10.1175/2009bams2755.1, 2010.

Lellouche, J.-M., Greiner, E., Bourdallé-Badie, R., Garric, G., Melet, A., Drévillon, M., Bricaud, C., Hamon, M., Le Galloudec, O., Regnier, C., Candela, T., Testut, C.-E., Gasparin, F., Ruggiero, G., Benkiran, M., Drillet, Y., and Le Traon, P.-Y.: The Copernicus global 1/12 oceanic and sea ice GLORYS12 reanalysis, Front. Earth Sci., 9, 698876, https://doi.org/10.3389/feart.2021.698876, 2021.

Liu, Y., Guan, S., Zhao, W., Liu, P., and Wang, C.: Dynamic modulation of storm size on upper ocean temperature response to tropical cyclones, J. Phys. Oceanogr., https://doi.org/10.1175/JPO-D-25-0125.1, 2025.

Liu, Z., Xu, J., Zhu, B., Sun, C., and Zhang, L.: The upper ocean response to tropical cyclones in the northwestern Pacific analyzed with Argo data, Chin. J. Oceanol. Limnol., 25, 123-131, https://doi.org/10.1007/s00343-007-0123-8, 2007.

Liu, Z., Li, Z., Lu, S., Wu, X., Sun, C., and Xu, J.: Scattered dataset of global ocean temperature and salinity profiles from the international Argo program, J. Glob. Change Data Discov., 5, 312-321, https://doi.org/10.3974/geodp.2021.04.03, 2021.

Ma, Z., Yan, X., and Fei, J.: Quantifying the Rightward Bias Extent of Tropical Cyclones' Cold Wakes, Geophys. Res. Lett., 50, e2023GL104578, https://doi.org/10.1029/2023gl104578, 2023.

Maue, R. N.: Recent historically low global tropical cyclone activity, Geophys. Res. Lett., 38, L14803, https://doi.org/10.1029/2011gl047711, 2011.

McTaggart-Cowan, R., Davies, E. L., Fairman Jr., J. G., Galarneau Jr., T. J., and Schultz, D. M.: Revisiting the 26.5 C sea surface temperature threshold for tropical cyclone development, Bull. Am. Meteorol. Soc., 96, 1929-1943, https://doi.org/10.1175/BAMS-D-13-00254.1, 2015.

Mei, W. and Pasquero, C.: Spatial and Temporal Characterization of Sea Surface Temperature Response to Tropical Cyclones, J. Clim., 26, 3745-3765, https://doi.org/10.1175/jcli-d-12-00125.1, 2013.

Park, K.-A., Park, J.-J., and Tang, W.: Oceanic response to typhoons in the Northwest Pacific using Aquarius and SMAP data (2011–2020), Front. Mar. Sci., 9, https://doi.org/10.3389/fmars.2022.1037029, 2023.

Pasquero, C. and Emanuel, K.: Tropical cyclones and transient upper-ocean warming, J. Clim., 21, 149-162, https://doi.org/10.1175/2007JCLI1550.1, 2008.

Pasquero, C., Desbiolles, F., and Meroni, A. N.: Air-Sea Interactions in the Cold Wakes of Tropical Cyclones, Geophys. Res. Lett., 48, https://doi.org/10.1029/2020gl091185, 2021.

Price, J. F.: Upper ocean response to a hurricane, J. Phys. Oceanogr., 11, 153-175, https://doi.org/10.1175/1520-0485(1981)011<0153:UORTAH>2.0.CO;2, 1981.

Price, J. F., Morzel, J., and Niiler, P. P.: Warming of SST in the cool wake of a moving hurricane, J. Geophys. Res., 113, https://doi.org/10.1029/2007jc004393, 2008.

Qiu, Y., Han, W., Lin, X., West, B. J., Li, Y., Xing, W., Zhang, X., Arulananthan, K., and Guo, X.: Upper-Ocean Response to the Super Tropical Cyclone Phailin (2013) over the Freshwater Region of the Bay of Bengal, J. Phys. Oceanogr., 49, 1201-1228, https://doi.org/10.1175/jpo-d-18-0228.1, 2019.

Reul, N., Quilfen, Y., Chapron, B., Fournier, S., Kudryavtsev, V., and Sabia, R.: Multisensor observations of the Amazon-Orinoco river plume interactions with hurricanes, J. Geophys. Res.-Oceans, 119, 8271-8295, https://doi.org/10.1002/2014jc010107, 2014.

Reul, N., Chapron, B., Grodsky, S. A., Guimbard, S., Kudryavtsev, V., Foltz, G. R., and Balaguru, K.: Satellite Observations of the Sea Surface Salinity Response to Tropical Cyclones, Geophys. Res. Lett., 48, https://doi.org/10.1029/2020gl091478, 2021.

Riser, S. C., Freeland, H. J., Roemmich, D., Wijffels, S., Troisi, A., Belbéoch, M., Gilbert, D., Xu, J. P., Pouliquen, S., Thresher, A., Le Traon, P. Y., Maze, G., Klein, B., Ravichandran, M., Grant, F., Poulain, P. M., Suga, T., Lim, B., Sterl, A., Sutton, P., Mork, K. A., Vélez-Belch, P. J., Ansorge, I., King, B., Turton, J., Baringer, M., and Jayne, S. R.: Fifteen years of ocean observations with the global Argo array, Nat. Clim. Change, 6, 145-153, https://doi.org/10.1038/Nclimate2872, 2016.

Roemmich, D., Johnson, G. C., Riser, S., Davis, R., Gilson, J., Owens, W. B., Garzoli, S. L., Schmid, C., and Ignaszewski, M.: The Argo Program Observing the Global Ocean with Profiling Floats, Oceanography, 22, 34-43, https://doi.org/10.5670/oceanog.2009.36, 2009.

Roemmich, D., Alford, M. H., Claustre, H., Johnson, K., King, B., Moum, J., Oke, P., Owens, W. B., Pouliquen, S., Purkey, S., Scanderbeg, M., Suga, T., Wijffels, S., Zilberman, N., Bakker, D., Baringer, M., Belbeoch, M., Bittig, H. C., Boss, E., Calil, P., Carse, F., Carval, T., Chai, F., Conchubhair, D. Ó., d'Ortenzio, F., Dall'Olmo, G., Desbruyeres, D., Fennel, K., Fer, I., Ferrari, R., Forget, G., Freeland, H., Fujiki, T., Gehlen, M., Greenan, B., Hallberg, R., Hibiya, T., Hosoda, S., Jayne, S., Jochum, M., Johnson, G. C., Kang, K., Kolodziejczyk, N., Körtzinger, A., Traon, P.-Y. L., Lenn, Y.-D., Maze, G., Mork, K. A., Morris, T., Nagai, T., Nash, J., Garabato, A. N., Olsen, A., Pattabhi, R. R., Prakash, S., Riser, S., Schmechtig, C., Schmid, C., Shroyer, E., Sterl, A., Sutton, P., Talley, L., Tanhua, T., Thierry, V., Thomalla, S., Toole, J., Troisi, A., Trull, T. W., Turton, J., Velez-Belchi, P. J., Walczowski, W., Wang, H., Wanninkhof, R., Waterhouse, A. F., Waterman, S., Watson, A., Wilson, C., Wong, A. P. S., Xu, J., and Yasuda, I.: On the Future of Argo: A Global, Full-Depth, Multi-Disciplinary Array, Front. Mar. Sci., 6, 439, https://doi.org/10.3389/fmars.2019.00439, 2019.

Rogers, R. F.: Recent Advances in Our Understanding of Tropical Cyclone Intensity Change Processes from Airborne Observations, Atmosphere, 12, 650, https://doi.org/10.3390/atmos12050650, 2021.

Sala, J., Giglio, D., Hu, A., Kuusela, M., Wood, K. M., and Lee, A. B.: Upper-ocean changes with hurricane-strength wind events: a study using Argo profiles and an ocean reanalysis, Ocean Sci., 20, 1441-1455, https://doi.org/10.5194/os-20-1441-2024, 2024.

Shay, L. K.: Air-sea interactions in tropical cyclones, in: Global Perspectives on Tropical Cyclones: From Science to Mitigation, World Scientific, 93-131, https://doi.org/10.1142/9789814293488_0003, 2010.

Shay, L. K., Jaimes, B., and Halliwell, G. R.: The Response of Quasigeostrophic Oceanic Vortices to Tropical Cyclone Forcing, J. Phys. Oceanogr., 41, 1965-1985, https://doi.org/10.1175/jpo-d-11-06.1, 2011.

Steffen, J. and Bourassa, M.: Barrier Layer Development Local to Tropical Cyclones based on Argo Float Observations, J. Phys. Oceanogr., 48, 1951-1968, https://doi.org/10.1175/jpo-d-17-0262.1, 2018.

Stiles, B. W., Portabella, M., Yang, X., and Zheng, G.: Editorial for Special Issue "Tropical Cyclones Remote Sensing and Data Assimilation", Remote Sens., 12, 3067, https://doi.org/10.3390/rs12183067, 2020.

Sun, J., Vecchi, G., and Soden, B.: Sea Surface Salinity Response to Tropical Cyclones Based on Satellite Observations, Remote Sens., 13, https://doi.org/10.3390/rs13030420, 2021a.

Sun, J., Vecchi, G. A., and Soden, B. J.: Influence of Vertical Wind Shear on the Ocean Response to Tropical Cyclones Based on Satellite Observations, Geophys. Res. Lett., 48, https://doi.org/10.1029/2021gl095451, 2021b.

van Haren, H., Chi, W.-C., Yang, C.-F., Yang, Y.-J., and Jan, S.: Deep sea floor observations of typhoon driven enhanced ocean turbulence, Prog. Oceanogr., 184, 102315, https://doi.org/10.1016/j.pocean.2020.102315, 2020.

Vincent, E. M., Lengaigne, M., Vialard, J., Madec, G., Jourdain, N. C., and Masson, S.: Assessing the

https://doi.org/10.5194/essd-2026-520
Preprint. Discussion started: 27 July 2026

Open Access Earth System Science Data Discussions

oceanic control on the amplitude of sea surface cooling induced by tropical cyclones, J. Geophys. Res.-Oceans, 117, https://doi.org/10.1029/2011jc007705, 2012a.

Vincent, E. M., Lengaigne, M., Madec, G., Vialard, J., Samson, G., Jourdain, N. C., Menkes, C. E., and Jullien, S.: Processes setting the characteristics of sea surface cooling induced by tropical cyclones, J. Geophys. Res.-Oceans, 117, https://doi.org/10.1029/2011jc007396, 2012b.

Wang, C., Wang, B., and Cao, J.: Unprecedented Northern Hemisphere Tropical Cyclone Genesis in 2018 Shaped by Subtropical Warming in the North Pacific and the North Atlantic, Geophys. Res. Lett., 46, 13327-13337, https://doi.org/10.1029/2019gl085406, 2019.

Wang, G., Wu, L., Johnson, N. C., and Ling, Z.: Observed three-dimensional structure of ocean cooling induced by Pacific tropical cyclones, Geophys. Res. Lett., 43, 7632-7638, https://doi.org/10.1002/2016gl069605, 2016.

Wang, G., Wu, L., Mei, W., and Xie, S. P.: Ocean currents show global intensification of weak tropical cyclones, Nature, 611, 496-500, https://doi.org/10.1038/s41586-022-05326-4, 2022.

Wang, X., Li, J., Sun, L., Xu, M., Liu, H., and Liu, R.: Competition between ocean thermal structure and tropical cyclone characteristics modulates ocean environmental responses in the Yellow and Bohai Seas, Mar. Environ. Res., 196, 106444, https://doi.org/10.1016/j.marenvres.2024.106444, 2024.

Wang, X., Li, J., Zhang, H., and Lian, T.: Latitudinal distributions of tropical cyclone-induced sea surface temperature cooling in the Northwestern Pacific (2003–2022), Clim. Dyn., 64, 106, https://doi.org/10.1007/s00382-026-08097-0, 2026a.

Wang, X., Zhang, H., Xu, M., Lian, T., Li, J., Tian, D., and Yu, J.: A Global Paired Argo Dataset for Ocean Thermal and Salinity Responses to Tropical Cyclones (2000–2024) [dataset], https://doi.org/10.6084/m9.figshare.32820563, 2026b.

Wang, Y. and Xiu, P.: Typhoon footprints on ocean surface temperature and chlorophyll-a in the South China Sea, Sci. Total Environ., 840, 156686, https://doi.org/10.1016/j.scitotenv.2022.156686, 2022.

Wentz, F. J., Gentemann, C., Smith, D., and Chelton, D.: Satellite measurements of sea surface temperature through clouds, Science, 288, 847-850, https://doi.org/10.1126/science.288.5467.847, 2000.

Wong, A. P. S., Wijffels, S. E., Riser, S. C., Pouliquen, S., Hosoda, S., Roemmich, D., Gilson, J., Johnson, G. C., Martini, K., Murphy, D. J., Scanderbeg, M., Bhaskar, T. V. S. U., Buck, J. J. H., Merceur, F., Carval, T., Maze, G., Cabanes, C., André, X., Poffa, N., Yashayaev, I., Barker, P. M., Guinehut, S., Belbéoch, M., Ignaszewski, M., Baringer, M. O. N., Schmid, C., Lyman, J. M., McTaggart, K. E., Purkey, S. G., Zilberman, N., Alkire, M. B., Swift, D., Owens, W. B., Jayne, S. R., Hersh, C., Robbins, P., West-Mack, D., Bahr, F., Yoshida, S., Sutton, P. J. H., Cancouët, R., Coatanoan, C., Dobbler, D., Juan, A. G., Gourrion, J., Kolodziejczyk, N., Bernard, V., Bourlès, B., Claustre, H., D'Ortenzio, F., Le Reste, S., Le Traon, P.-Y., Rannou, J.-P., Saout-Grit, C., Speich, S., Thierry, V., Verbrugge, N., Angel-Benavides, I. M., Klein, B., Notarstefano, G., Poulain, P.-M., Vélez-Belchí, P., Suga, T., Ando, K., Iwasaska, N., Kobayashi, T., Masuda, S., Oka, E., Sato, K., Nakamura, T., Sato, K., Takatsuki, Y., Yoshida, T., Cowley, R., Lovell, J. L., Oke, P. R., van Wijk, E. M., Carse, F., Donnelly, M., Gould, W. J., Gowers, K., King, B. A., Loch, S. G., Mowat, M., Turton, J., Rama Rao, E. P., Ravichandran, M., Freeland, H. J., Gaboury, I., Gilbert, D., Greenan, B. J. W., Ouellet, M., Ross, T., Tran, A., Dong, M., Liu, Z., Xu, J., Kang, K., Jo, H., Kim, S.-D., and Park, H.-M.: Argo Data 1999–2019: Two Million Temperature-Salinity Profiles and Subsurface Velocity Observations

https://doi.org/10.5194/essd-2026-520
Preprint. Discussion started: 27 July 2026

Earth System Science Data Discussions
Open Access

From a Global Array of Profiling Floats, Front. Mar. Sci., 7, 700, https://doi.org/10.3389/fmars.2020.00700, 2020.

Wu, Q. and Chen, D.: Typhoon-Induced Variability of the Oceanic Surface Mixed Layer Observed by Argo Floats in the Western North Pacific Ocean, Atmos.-Ocean, 50, 4-14, https://doi.org/10.1080/07055900.2012.712913, 2012.

Xu, M., Wang, X., Sun, L., Liu, H., Liu, R., and Lu, G.: Composited sea surface responses to tropical cyclones in the Bay of Bengal during 2003-2020, Mar Environ Res, 202, 106779, https://doi.org/10.1016/j.marenvres.2024.106779, 2024.

Zhang, H., Chen, D., Zhou, L., Liu, X., Ding, T., and Zhou, B.: Upper ocean response to typhoon Kalmaegi (2014), J. Geophys. Res.-Oceans, 121, 6520-6535, https://doi.org/10.1002/2016jc012064, 2016.

Zhang, H., He, H., Zhang, W.-Z., and Tian, D.: Upper ocean response to tropical cyclones: a review, Geosci. Lett., 8, https://doi.org/10.1186/s40562-020-00170-8, 2021.

Zhang, H., Xie, X., Yang, C., Qi, Y., Tian, D., Xu, J., Cai, S., Wu, R., Ma, Y., Ni, X., and Chen, D.: Observed Impact of Typhoon Mangkhut (2018) on a Continental Slope in the South China Sea, J. Geophys. Res.-Oceans, 127, https://doi.org/10.1029/2022jc018432, 2022.

Zhang, H.: Modulation of Upper Ocean Vertical Temperature Structure and Heat Content by a Fast-Moving Tropical Cyclone, J. Phys. Oceanogr., 53, 493-508, https://doi.org/10.1175/jpo-d-22-0132.1, 2023.

Zhang, H., Tian, D., Sun, Y., Yang, M., Yang, S., Zhou, Y., Sun, X., and Chen, D.: Unmanned vehicles probed inner-core air-sea conditions during Super Typhoon Koinu (2023), Sci. Bull., https://doi.org/10.1016/j.scib.2024.10.018, 2024a.

Zhang, H., Chen, D., Liu, T., Tian, D., He, M., Li, Q., Wei, G., and Liu, J.: MASCS 1.0: synchronous atmospheric and oceanic data from a cross-shaped moored array in the northern South China Sea during 2014–2015, Earth Syst. Sci. Data, 16, 5665-5679, https://doi.org/10.5194/essd-16-5665-2024, 2024b.

Zhang, H., Li, Q., Chen, D., Shang, X., Tian, D., Liu, T., He, M., Hong, J., Wei, G., and Liu, J.: Atmospheric and oceanic data from a triangle-shaped moored array in the northern South China Sea during 2016, Sci. Data, 13, 467, https://doi.org/10.1038/s41597-026-06801-7, 2026.

Zhang, Z., Gao, J., Wang, J., and Wang, F.: Contributions of Tropical Cyclones and Internal Tides To Deep Near-Inertial Kinetic Energy Under Eddy Modulation, Geophys. Res. Lett., 51, https://doi.org/10.1029/2024gl111330, 2024c.

Zhao, W., Zhou, C., Zhang, Z., Huang, X., Guan, S., Yang, Q., Sun, Z., Qin, C., Guan, Y., and Tian, J.: The South China Sea Mooring Array and its applications in exploring oceanic multiscale dynamics, Sci. Bull., 70, 609-623, https://doi.org/10.1016/j.scib.2024.12.008, 2025.